Catalytic deep oxidation of NO by ozone over MnOx loaded spherical alumina catalyst

Fawei Lin, Zhihua Wang*, Qiang Ma, Ye Yang, Ronald Whiddon, Yanqun Zhu, Kefa Cen

State Key Laboratory of Clean Energy Utilization, Zhejiang University, Hangzhou 310027, PR China

ABSTRACT

The deep oxidation of NO by ozone, converting NO into N_2O_5, combined with wet flue gas treatment is an attractive method for simultaneously reduction of NO_x and SO_2 to ultra-low concentrations. However, the long residence time required, excessive ozone usage and consequent ozone leakage are serious problems for this technology. A catalyst of MnO_x loaded onto spherical alumina support material was prepared, which displayed excellent properties that would reduce the associated problems of deep oxidation of NO by ozone. Experiments performed with the stoichiometric O_3/NO_x ratio, 1.5, showed an NO_2 concentration reduction from 600 ppm to 100 ppm at 100 °C after 0.12 s residence time, and an ozone leakage of less than 20 ppm. The NO deep oxidation efficiency exceeded 95% for O_3/NO_x >1.57, and the catalyst showed good stability, even with SO_2. A mechanism for catalytic deep oxidation of NO by ozone was proposed, with two pathways based on the catalytic decomposition of ozone. In the first pathway, ozone is decomposed into active oxygen atoms on the catalyst surface; in the second pathway, the manganese(III) was oxidized into manganese(IV) and manganese(VII) by the decomposition of ozone. Subsequently, NO_2 adsorbed on the catalyst surface is oxidized by active oxygen atoms or oxidized manganese ions, generating NO_3 and nitrates. Finally, N_2O_5, formed by the combination of NO_2 and NO_3, is desorbed from the catalyst surface. The results of several characterizations, including XRD, XPS, H_2-TPR, TGA, TPD, FTIR, and BET, revealed that the second mechanism was the most dominant during the catalytic ozonation process. Additionally, the presence of ozone improved the catalyst adsorption of NO_x, and O_2, especially with exposure to SO_2, and demonstrated better performance regarding SO_2 poisoning than catalytic oxidation of NO by O_2.

1. Introduction

Nitrogen oxides (NO_x) are traditionally removed by selective catalytic reduction (SCR) [1,2] or selective non-catalytic reduction (SNCR) [3]. However, these removal methods have the strict temperature window and limited efficiency. With increasingly stringent nitrogen oxides emission standards, ultra-low emission levels are becoming more important. Recently, low temperature oxidation of NO by ozone [4–8] together with WFGD (wet flue gas desulfurization) has been proposed for efficiently simultaneous reduction of NO_x and SO_2 to ultra-low concentrations. During the process, insoluble NO (>95% of NO_x) is converted to NO_2 at an O_3/NO molar ratio <1.0 [8]. It was found that the NO_2 absorption efficiency was unsatisfactory in the limestone slurry [9]. As the solubility of nitrogen oxides increases with the valence state, N_2O_5,

which has the highest solubility among all nitrogen oxides, is more effectively absorbed than NO_2 during wet scrubbing [10,11]. Thus, excess ozone may be injected in an effort to further oxidize NO_2 to N_2O_5 with subsequent improvement to the NO_x removal efficiency [12]. This is referred to the deep oxidation of NO by ozone. Significant limitations in the deep oxidation of NO by ozone are the long residence time required (3–5 s) and excessive dosage of O_3 compared with stoichiometric ratio needed to promote efficient conversion of NO to N_2O_5, which also leads to O_3 leakage.

Ozone, due to its high oxidative ability, has been widely applied in the removal of organic compounds in water and air treatment [13,14]. Catalytic ozonation reduces the ozone requirement in comparison to direct oxidation with ozone [15,16]. Therefore, catalytic ozonation has been extensively investigated as a means to improve the ozone utilization rate in oxidative process [15–23]. Transition metal oxides (Mn, Fe, Ce, Co, Cu, Ni) [23–25] are commonly used in catalytic ozonation, with manganese oxides exhibiting the highest catalytic activity among these metals. Depositing the manganese oxide on a mechanical support material (Mn/SiO₂ [18],

* Corresponding author.
E-mail address: wangzh@zju.edu.cn (Z. Wang).

Nomenclature

Abbreviations

SCR	Selective catalytic reduction
SNCR	Selective non-catalytic reduction
WFGD	Wet flue gas desulfurization
EDS	Energy Dispersive Spectrometer
DBD	Dielectric Barrier Discharge
GHSV	Gas hourly space velocity
FTIR	Fourier transform infrared spectroscopy
XRD	X-ray diffraction
XPS	X-ray photoelectron spectroscopy
H_2-TPR	H_2-temperature programmed reduction
TGA	Thermal gravimetric analysis
DTA	Differential thermal analysis
TPD	Temperature programmed desorption
BET	A specific surface area calculated method named by Brunauer, Emmett, and Teller

Symbols

O_3/NO	The molar ratio of O_3 to NO_x

Mn/zeolite [19], Mn/USY [20], Mn/Al$_2$O$_3$ [21,22], Mn/activated carbon [26]) further improves oxidation efficiency [17]. Previous works confirmed that the catalytic ozonation properties were highly dependent on surface area but not the type of support [18]. The catalytic ozonation pathway for organic compounds proceeds by the adsorption of ozone and organic molecules on the catalyst followed by the decomposition of ozone to atomic oxygen which enhances dissociative radical formation and oxidation rate [15,22]. According to previous works [17–23], catalytic ozonation improved the conversion efficiency for organic compounds at lower temperature than conventional catalytic oxidation by O$_2$ [27]. However, catalyst deactivation by accumulation of by-product species which are not readily decomposed at lower temperature may appreciably reduce the catalyst operation [28].

In comparison to the non-catalytic ozone based NO deep oxidation, utilization of catalyst could shorten required reaction time and reduce the necessary ozone excess which will, in turn, reduce ozone leakage. Jõgi et al. [29] demonstrated increased efficiency of

NO deep oxidation with TiO$_2$ catalyst. However, the catalyst stability was neglected and the catalytic reaction process was uncovered through characterization measurements. To this end, a supported manganese oxide catalyst was prepared and evaluated as a means to improve the efficiency of ozone based NO deep oxidation. Supporting the catalyst on spherical alumina can alleviate the catalyst deactivation due to byproducts accumulation and increase the surface area which extended catalytic reaction time to enhance the deep oxidation rate. In addition to measuring the conversion efficiency of NO and NO$_2$ under different operating conditions, the catalyst was characterized using various analytical methods. Using the data from experiments, a probable ozone catalytic oxidation mechanism was created.

2. Experimental

2.1. Catalyst preparation

The catalyst consisting of MnO$_x$ loaded onto spherical alumina (2–3 mm diameter) was prepared by the impregnation method using analytical grade reagents (Sinopharm Chemical Reagent Co., Ltd.). A 50 g mass of spherical alumina was immersed in the deionized aqueous solution (30 mL) containing 11.14 g of Mn(CH$_3$COO)$_2$·4H$_2$O. The mixture was placed in an ultrasonic bath for 2 h and then left at room temperature for 24 h. The coated spherical alumina was then dried at 110 °C for 12 h, and subsequently calcined at 400 °C for 3 h under air atmosphere. The mass fraction of Mn in the final catalyst was approximately 5.39% as measured by the EDS (Energy Dispersive Spectrometer) method, which was slightly higher than the calculated theoretical mass fraction due to mass loss from the alumina support material during the preparation process.

2.2. Activity and stability tests

The catalytic activity and stability tests were carried out using the experimental setup shown in Fig. 1. The simulated flue gas was mixed from bottled gas supplied by Jingong Gas Co., Ltd. (N$_2$—99.999%, O$_2$—99.999%, NO—5%/balance N$_2$, SO$_2$—5%/balance N$_2$). The initial NO concentration was set around 600 ppm. Ozone was produced using a DBD (Dielectric Barrier Discharge) device
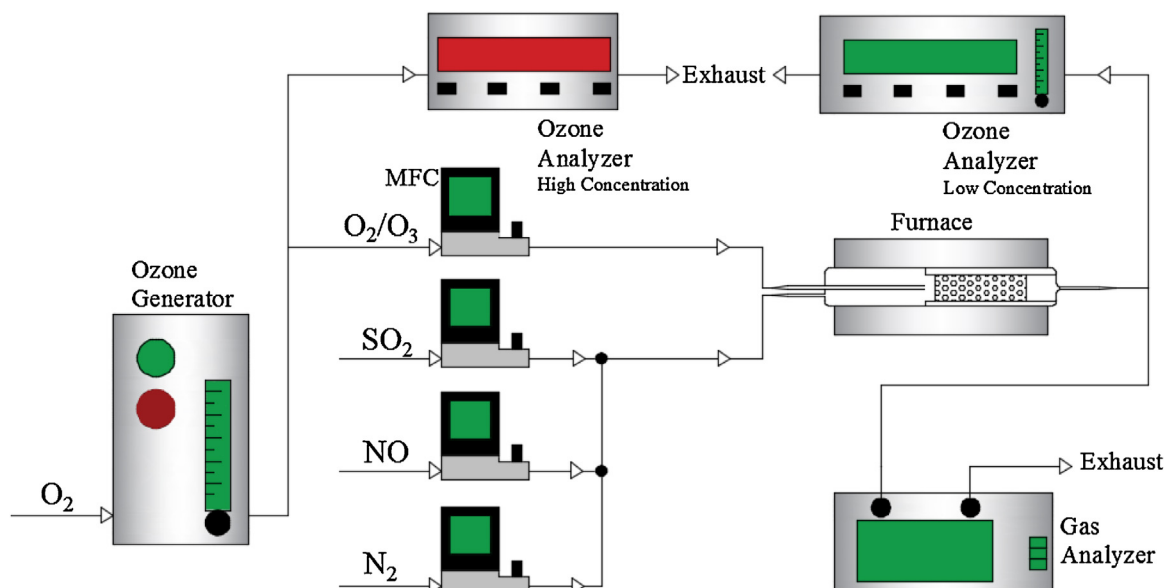

Fig. 1. Experimental setup for catalytic deep oxidation of NO and catalyst stability tests.

(Qingdao Guolin Co., model CF-G-3-10 g; >10 g/h); the O_3/O_2 and NO/N_2 gas streams were injected at separate locations in the reactor to prohibit reaction before entering the designated reactor volume. The total flow rate was 2 L/min with 5% oxygen, controlled by individual mass flow controllers (MFC, Alicat Scientific Inc.). 2.2 g of catalyst was loaded into the reaction chamber. The total residence time from introduction of the simulated flue gas and O_3/O_2 stream to sample analysis was 0.24 s, with a residence time of 0.12 s on the catalyst. The residence time in the FTIR cell is approximately 12 s. However, the analysis of FTIR is conducted immediately when the gas enters into the cell. Meanwhile, several times of tests had been conducted [30], and showed that the residence time in the FTIR cell has almost no impact on the results. Furthermore, it has been verified that the reaction has been carried out completely after the catalytic section and the later residence time has little impact on the results. As a result, the results of catalytic reaction are not affected by the FTIR cell. The corresponding GHSV (gas hour space velocity) is 30,000 h^{-1}. When assaying the catalyst resistance of SO_2 and water vapor, 200 ppm SO_2 and 10 vol.% of water vapor, respectively, were added to the simulated flue gas stream. The water vapor was added by bubbling in the simulated flue gas through water.

The catalyst was maintained at 100 °C using an electrically heated tube furnace (Yifeng furnace Co., Ltd.) unless specifically stated otherwise. The inlet ozone concentration was continuously monitored with an ozone analyzer (BMT-964 BT, OSTI Inc.; 0–200 g/Nm^3, ±0.1 g/Nm^3). A second ozone analyzer (Model 205, 2 B Technologies; 0–200 ppm ± 1 ppb) monitored the reactor outlet stream to determine the ozone leakage. The concentrations of N_2O, NO, NO_2, SO_2, H_2O and O_2 in the outlet gas stream were measured by an FTIR (Fourier transform infrared spectroscopy) gas analyzer

(DX4000, Gasmet). The N_2O_5 and NO_3 formation was deduced from the infrared absorption spectra obtained from the FTIR analyzer. All the tests in this paper were carried out after the adsorption of NO mixture for 1 h to obtain the stable outlet concentrations. The conversion efficiency was described by the determined by the molar loss in NO and NO_2, which as defined in Eq. (1).

$$[\text{Conv.}] = (1 - ([NO]_{out} + [NO_2]_{out})/([NO]_{initial} + [NO_2]_{initial})) \times 100\% \qquad (1)$$

where [Conv.] is the conversion efficiency, $[NO]_{out}$ and $[NO_2]_{out}$ are the outlet concentration of NO and NO_2, respectively, $[NO]_{initial}$ and $[NO_2]_{initial}$ are the initial concentration of NO and NO_2, respectively.

The catalytic decomposition of ozone was measured using the same system and parameters. The initial ozone concentration was about 600 ppm. The ozone decomposition efficiency was calculated by Eq. (2).

$$[\text{Deco.}] = (1 - [O_3]_{out}/[O_3]_{initial}) \times 100\% \qquad (2)$$

where [Deco.] is the decomposition efficiency, $[O_3]_{out}$ and $[O_3]_{initial}$ are ozone concentration measured at the reaction chamber inlet and outlet, respectively.

2.3. Catalyst characterization

The catalyst was characterized using XRD (X-ray diffraction), XPS (X-ray photoelectron spectroscopy), H_2-TPR (H_2-temperature programmed reduction), TGA (Thermal gravimetric analysis), TPD (Temperature programmed desorption), FTIR (Fourier transform infrared spectroscopy), specific surface area and pore structure measurements. These analyses were applied to catalyst samples
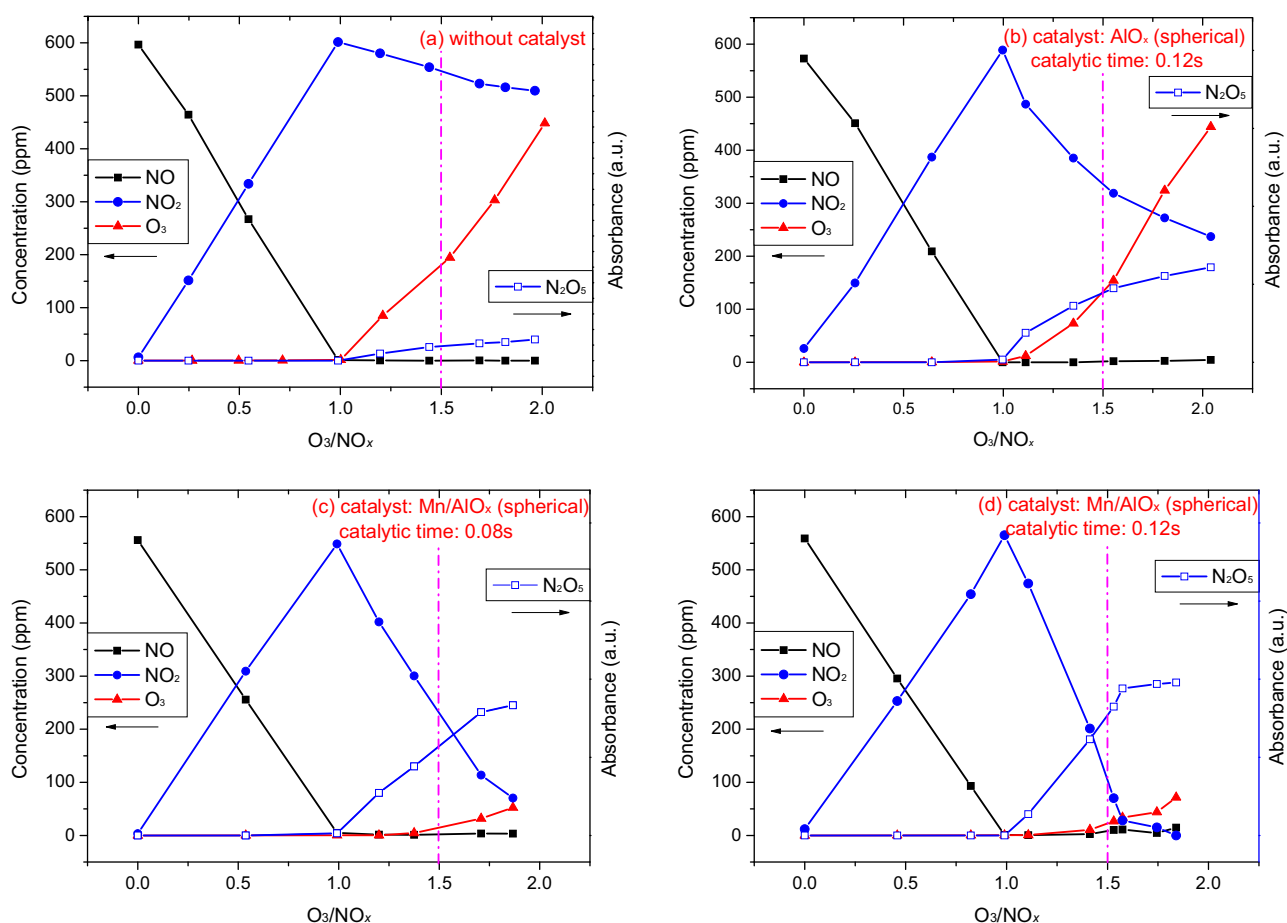

Fig. 2. NO oxidation process with or without MnO$_x$ loaded spherical alumina catalyst.

that had undergone various stages of use: (A) fresh catalyst, (B) catalyst after ozone decomposition for 200 min, (C) catalyst after deep oxidation without SO_2 for 200 min, (D) catalyst after deep oxidation with SO_2 for 200 min, (E) spherical alumina, (F) catalyst after adsorption of NO and O_2 for 200 min, (G) catalyst after adsorption of NO, SO_2 and O_2 for 200 min. Hereafter, samples will be referred to by letter for simplification.

The XRD patterns were collected using a Rigaku D/max 2550PC diffractometer with Cu Kα radiation. The XPS spectra were recorded with a photoelectron spectrometer (Thermo Scientific Escalab 250Xi) with a standard Al Kα source (1486.6 eV). All binding energies were referenced to the C 1 s line at 284.5 eV. H_2-TPR and TPD measurements were conducted using an automatic temperature programmed chemisorption analyzer (Micromeritics AutoChem II 2920). For H_2-TPR, 50 mg catalyst samples were pretreated at 200 °C for 90 min. For TPD, 50 mg catalyst samples were heated at 70 °C for 30 min to remove adsorbed water. After pretreatment, the samples were heated to the target temperature at a rate of 10 °C/min under N_2 atmosphere. The TCD signals of NO, NO_2, O_2, and SO_2 were obtained by a Hiden QIC20 mass spectrometer. TGA and DTA (differential thermal analysis) curves were obtained with a thermo-gravimetric analyzer (TA-Q500 TGA); the temperature was increased to 1000 °C at a rate of 10 °C/min under N_2 atmosphere. FTIR spectra were measured by a Nicolet 5700 FTIR spectrometer with 0.09 cm^{-1} resolution. The catalysts porous structure parameters were determined by BET method through N_2 adsorption using a Micromeritics ASAP 2010 analyzer at 77 K.

3. Results and discussion

3.1. Catalytic deep oxidation of NO by ozone

3.1.1. Catalytic properties

From the global reaction ($2NO + 3O_3 = N_2O_5 + 3O_2$) for N_2O_5 formation, the stoichiometric ratio of ozone to NO is 1.5; catalytic deep oxidation of NO by ozone aims at maximizing the N_2O_5 formation efficiency at the stoichiometric ozone NO ratio. To validate the activity of manganese oxides catalyst, the absorbance of N_2O_5 and residual concentrations of NO, NO_2, and O_3 were measured without catalyst, with bare spherical alumina support and with Mn catalyst on the spherical alumina support (Fig. 2). It can be seen from Fig. 2(a) that in direct reaction between NO and ozone, the NO_2 concentration decreases by 50 ppm as the O_3/NO_x ratio is increased from 1.0 to 1.5, with little residual NO. Over the same variation in O_3/NO_x ratio, the NO_2 concentration declines 280 ppm for spherical alumina (Fig. 2(b)), a large increase in conversion due to the large surface area of spherical alumina.

When manganese oxide was loaded onto the spherical alumina support, the NO_2 concentration declines markedly as shown in Fig. 2(c)–(d). When the catalyst was compacted to reduce the residence time, the efficiency of stoichiometric NO_2 deep oxidation decreases from 83.1% (0.12 s residence time) to 67.6% (0.08 s residence time). Obviously, correct matching of the flue gas residence time to the catalyst reaction rate is important to the efficiency of the deep NO oxidation process. The peak NO deep oxidation efficiency exceeds 95% for O_3/NO_x above 1.57 in the 0.12 s residence case. At these conditions, N_2O and NO_3 are minority products that are barely detectible.

Ozone leakage at the stoichiometric ratio of $O_3/NO_x = 1.5$ declines from 150 ppm without catalyst to less than 20 ppm when using the MnO_x loaded spherical alumina catalyst.

The catalytic ozonation process is expected to proceed by the decomposition of ozone on the catalyst surface. This decomposition of ozone occurs by two possible pathways: the first pathway is shown in Eqs. (3)–(5) [31,32], whereby active oxygen atoms are
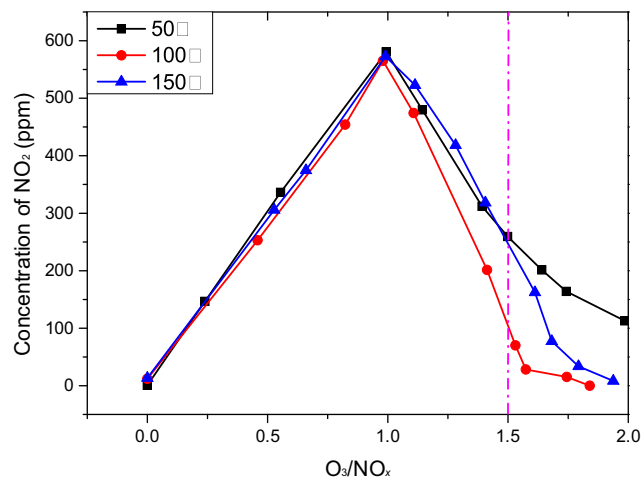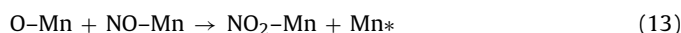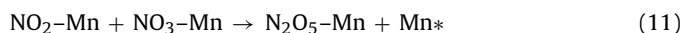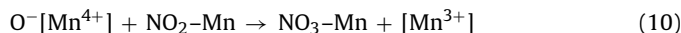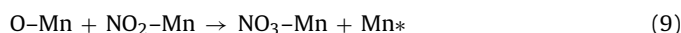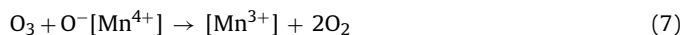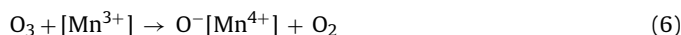

Fig. 3. The NO_2 concentrations with variation of O_3/NO_x at different temperatures.

generated; the second pathway is shown in Eqs. (6)–(8) [33,34], which involves the transition of the Mn valance state. In the reactions, "Mn*" indicates an open catalyst active site while "–Mn" represents an atom or molecule adsorbed at the catalyst site. Similarly, the proposed mechanism for catalytic deep oxidation of NO by ozone also includes two pathways, with the only difference regarding NO_3 formation. Active oxygen (Eq. (3)) or oxidized manganese(IV) (Eq. (6)) reacts with NO_2–Mn generating NO_3–Mn through Eqs. (9) and (10). The NO_3–Mn combines with NO_2–Mn to form N_2O_5–Mn through Eq. (11). Finally, the N_2O_5 will be desorbed from catalyst surface (Eq. (12)), and the catalytic ozonation cycle for N_2O_5 formation is terminated. Since there is NO in the gas supply, active oxygen atoms or manganese(IV) may react with NO–Mn generating NO_2–Mn via Eqs. (13) and (14).

$$O_3 + Mn_* \rightarrow O_2 + O\text{–}Mn \tag{3}$$

$$O_3 + O\text{–}Mn \rightarrow O_2 + O_2\text{–}Mn \tag{4}$$

$$O_2\text{–}Mn \rightarrow O_2 + Mn_* \tag{5}$$

$$O_3 + [Mn^{3+}] \rightarrow O^-[Mn^{4+}] + O_2 \tag{6}$$

$$O_3 + O^-[Mn^{4+}] \rightarrow [Mn^{3+}] + 2O_2 \tag{7}$$

$$2O^-[Mn^{4+}] \rightarrow 2[Mn^{3+}] + O_2 \tag{8}$$

$$O\text{–}Mn + NO_2\text{–}Mn \rightarrow NO_3\text{–}Mn + Mn_* \tag{9}$$

$$O^-[Mn^{4+}] + NO_2\text{–}Mn \rightarrow NO_3\text{–}Mn + [Mn^{3+}] \tag{10}$$

$$NO_2\text{–}Mn + NO_3\text{–}Mn \rightarrow N_2O_5\text{–}Mn + Mn_* \tag{11}$$

$$N_2O_5\text{–}Mn \rightarrow N_2O_5 + Mn_* \tag{12}$$

$$O\text{–}Mn + NO\text{–}Mn \rightarrow NO_2\text{–}Mn + Mn_* \tag{13}$$

$$O^-[Mn^{4+}] + NO\text{–}Mn \rightarrow NO_2\text{–}Mn + [Mn^{3+}] \tag{14}$$

3.1.2. Effect of catalytic reaction temperature

The influence of temperature on the catalytic deep oxidation of NO by ozone was investigated at 50 °C, 100 °C, and 150 °C. The results (Fig. 3) show that the NO_2 concentration at 100 °C is lower than when running the catalyst at either higher or lower temperature. In the reaction pathway above, intermediate species accumulate on the catalyst surface during catalytic ozonation process. When the temperature is 50 °C, the byproducts accumulated on the catalyst surface cannot desorb rapidly, resulting in the active sites always be occupied, cannot be regenerated. Thus, the NO_2 concentration declines when the temperature is raised from 50 °C to 100 °C, as the rate of desorption increases. According to previous
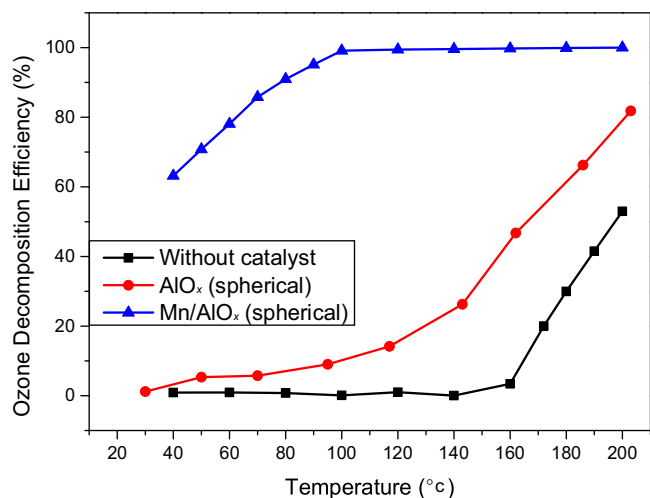
Fig. 4. Catalytic properties for ozone decomposition.

work [12], the NO_3 and N_2O_5 will be substantially decomposed at higher temperature. Additionally, ozone decomposition will also be accelerated at higher temperature reducing available active oxygen atoms for NO deep oxidation. Therefore, he NO_2 concentration increases when the temperature increases to 150 °C. Above all, the lower catalytic property at lower temperature is attributed to the accumulation of byproducts, while that at higher temperature is attributed to the thermodynamic decomposition of NO_3, N_2O_5, and O_3.

3.1.3. Catalytic decomposition of ozone

In the catalytic NO deep oxidation mechanism described above, ozone decomposition on the catalyst surface is an important initiation step. The efficiencies of ozone decomposition with and without catalyst are shown in Fig. 4. Absent a catalyst, ozone does not show appreciable decomposition when the temperature is lower than 160 °C. Even as the temperature increases to 200 °C, the decomposition efficiency only reaches 53%. For spherical alumina support material, the decomposition of ozone begins from 30 °C and the efficiency is slightly higher than the non-catalyst case at all temperatures. Ozone decomposition efficiency with MnO_x loaded spherical alumina is much higher than the preceding two cases and reaches 100% at 100 °C. The reactions for ozone decomposition on manganese oxide catalyst are listed as Eqs. (3)–(5) and (6)–(8). It has been found that the rates of these steps are equal at steady state [35]. During ozone decomposition, catalysts undergo repeated oxidation and reduction cycles [36]. The manganese oxides are more reducible than other oxides [37,38] and have easily accessible multiple oxidation states that can be the excellent catalyst for ozone decomposition [35].

3.2. Catalyst stability

Catalyst stability is an important property when considering real world applications and accurate costing of catalytic treatment solutions. The catalyst stability for NO deep oxidation with ozone in 600 ppm NO gas was tested at $O_3/NO_x = 1.57$, shown in Fig. 5(a). The conversion efficiency showed a slight decrease over the test's 200 min duration though the efficiency remained near 90%. This may be improved by optimization of the diameter of spherical alumina and reaction temperature in the future.

In addition to NO, there are various other compounds in the real flue gas, such as SO_2 and water vapor, which may lead to catalyst deactivation [39,40]. For this reason, the catalyst stabilities were assessed with either 200 ppm SO_2 or 10 vol.% water
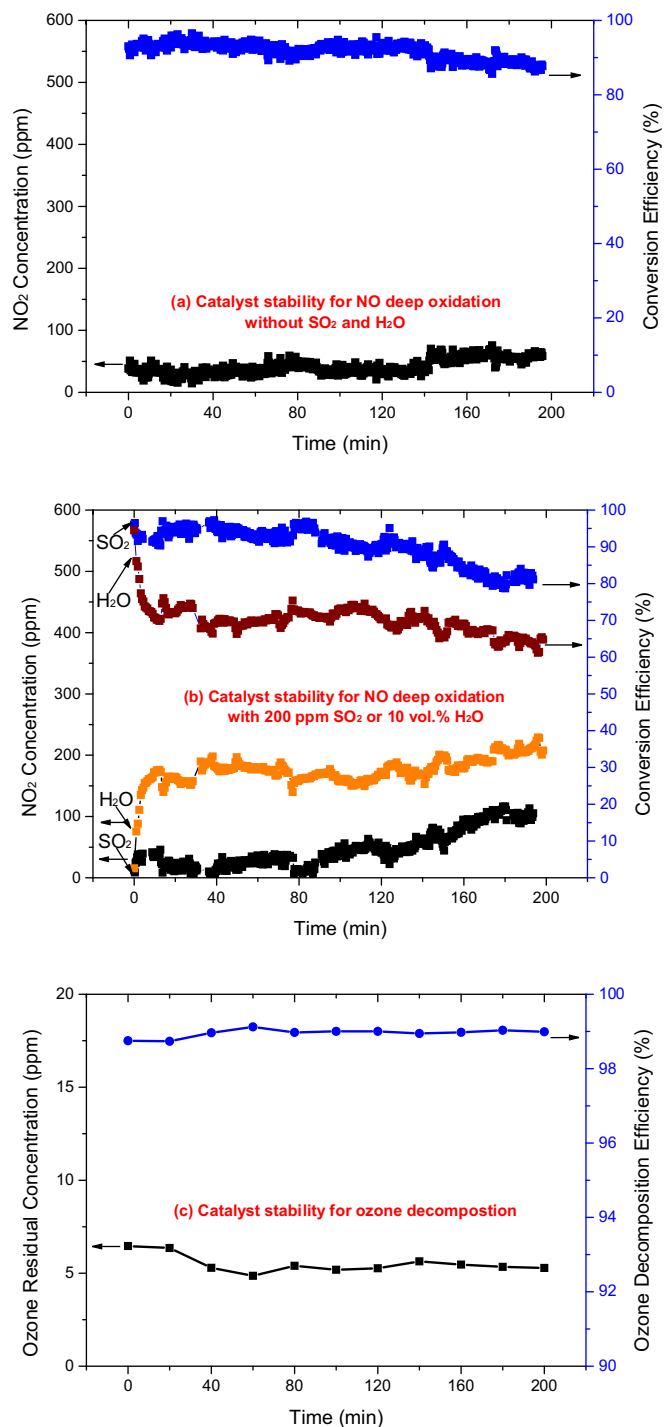

Fig. 5. Catalyst stabilities for NO deep oxidation and ozone decomposition.

vapor added to the NO sample gas, at an $O_3/NO_x = 1.57$. The results are shown in Fig. 5(b). When SO_2 was added, it can be observed that the NO_2 conversion decreases more noticeably than the neat NO/N_2 gas in Fig. 5(a), especially after 120 min. The conversion efficiency decreases to near 80% with a residual NO_2 concentration of more than 100 ppm. This is still significantly better performance than what is found in the catalysts for NO oxidation by O_2 [41]. One explanation for the better performance regarding SO_2 poisoning is that the use of ozone may renovate catalytic sites that have been inactivated. The mechanism of SO_2 passivation will be discussed later. When water vapor was added, the conversion efficiency decreases sharply to 70% and the residual NO_2 concentration

exceeds 170 ppm after just 10 min with slight change thereafter. This loss of catalyst efficiency may be attributed to a decrease in surface area caused by the presence of water vapor, which will be investigated at a future time.

Fig. 5(c) shows the catalyst stability for ozone decomposition at 100 °C, no significant decline was observed over the test duration. The various literatures report dealing with ozone decomposition on manganese oxide catalysts, giving disparate results regarding catalyst stability during ozone decomposition. Manganese oxides supported on γ-Al₂O₃ remained stable for 120 min as reported by Einaga et al. [42]. Wang et al. [43] studied ozone decomposition over MnO_x supported on activated carbon and reported that the decomposition ratio declined quickly in the first few minutes due to the adsorption on the catalyst. This may indicate the support material as being determinant in the susceptibility of Mn catalyst degradation in ozone loaded environments.

3.3. Catalyst characterization

In order to further investigate the catalytic mechanism for the deep oxidation of NO by ozone, the catalyst was characterized using XRD, XPS, H₂-TPR, TGA, TPD, FTIR, and BET measurements. The experiments were conducted on catalyst samples after different aging as outlined in Section 2.3.

3.3.1. XRD

XRD patterns for the catalyst support material and the catalyst after different usage are shown in Fig. 6. For the bare spherical alumina sample (curve (E)), the diffraction spectrum is complicated with several peaks attributable to bohmite AlO(OH), gibbsite Al(OH)₃, and Al₂O₃. For the unused catalyst (curve (A)), only the diffraction peaks related to aluminum compounds can be detected. The gibbsite peaks completely disappear and bohmite peaks are weakened; likewise, the diffraction peaks corresponding to Al₂O₃ are strengthened. This indicates that manganese oxides have been highly dispersed on the spherical alumina substrate and that the calcination process has yielded a phase transition. The three catalyst samples aged with different conditions (NO, NO + SO₂, O₃) showed almost no difference in the diffraction spectra as compared to the unused catalyst. It can be concluded that the catalytic reaction process does not degrade the catalyst structure and that the intermediate species formation occurs at the catalyst surface.

3.3.2. XPS

The XPS spectra of the catalyst samples were collected to probe changes in the active sites that may occur during the catalytic deep oxidation process. Fig. 7(a) shows the Mn 2p profiles, including a spin orbit doublet with Mn 2p₃/₂ and Mn 2p₁/₂ observed at 642 eV and 653 eV, respectively. The Mn 2p₃/₂ region is resolved into subbands using the optimum combination of Gaussian peaks method. The binding energies and the valance state ratios of Mn in the catalyst samples are given in Table 1. Peaks corresponding to Mn^{3+} and Mn^{4+} [44] due to the interaction between manganese and aluminum oxides can be found for fresh catalyst (curve (A)), catalyst after deep oxidation of NO without SO₂ (curve (C)) and with SO₂ (curve (D)). An additional peak assigned to Mn^{7+} [45,46] can be detected for the catalyst sample after ozone decomposition (curve
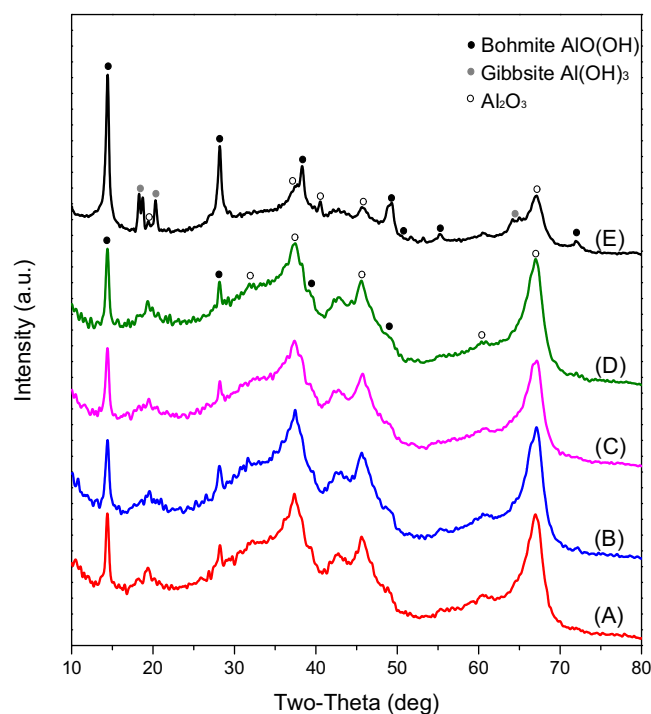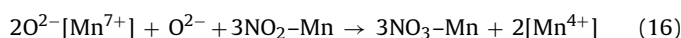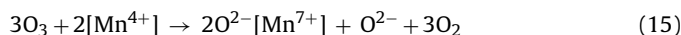

Fig. 6. XRD patterns for fresh Mn/AlO_x catalyst (A), after ozone decomposition (B), after deep oxidation without SO₂ (C), after deep oxidation with SO₂ (D), and spherical alumina (E).

(B)) and the ratio of Mn^{4+} increases, implying that Mn was oxidized by ozone through Eqs. (6) and (15). Reed et al. [47] also noted the electron transfer from catalyst to ozone causing ozone decomposition into active oxygen. Comparing sample (A) and sample (C) in Table 1, no discrepancy can be seen for the ratios of Mn^{3+} and Mn^{4+} after catalytic deep oxidation of NO by ozone. It can be deduced that oxidized manganese oxides are consumed through Eqs. (10) and (16) of the deep oxidation process. However, addition of SO₂ to the NO/N₂ stream causes a decline in the Mn^{4+} after deep oxidation (sample (D)). SO₂ acts analogous to NO₂ in the catalytic cycles, through Eq. (17) where active Mn^{4+} is reduced. Also for the catalyst sample exposed to SO₂, an additional peak assigned to Mn^{2+} [48] appears, which is ascribed to Eq. (18).

$$3O_3 + 2[Mn^{4+}] \rightarrow 2O^{2-}[Mn^{7+}] + O^{2-} + 3O_2 \tag{15}$$

$$2O^{2-}[Mn^{7+}] + O^{2-} + 3NO_2-Mn \rightarrow 3NO_3-Mn + 2[Mn^{4+}] \tag{16}$$

$$O^-[Mn^{4+}] + SO_2-Mn \rightarrow SO_3-Mn + [Mn^{3+}] \tag{17}$$

$$O^-[Mn^{3+}] + SO_2-Mn \rightarrow SO_3-Mn + [Mn^{2+}] \tag{18}$$

The O 1s spectra, shown in Fig. 7(b), are deconvoluted into two peaks attributable to lattice oxygen O_α and chemisorbed oxygen O_β [49,50]; the integrated peak area ratios are listed in Table 2. It can be seen that the ratio of O_β/O_α declines from 1.30 to 1.07 after catalytic decomposition of ozone (sample (B)) as compared to fresh catalyst (sample (A)). As mentioned previously, ozone decomposition will generate active oxygen adsorbed on the catalyst surface via the first pathway, and conduct redox reactions of manganese oxides via the

Table 1
The Mn 2p₃/₂ binding energies (eV) and valance composition.

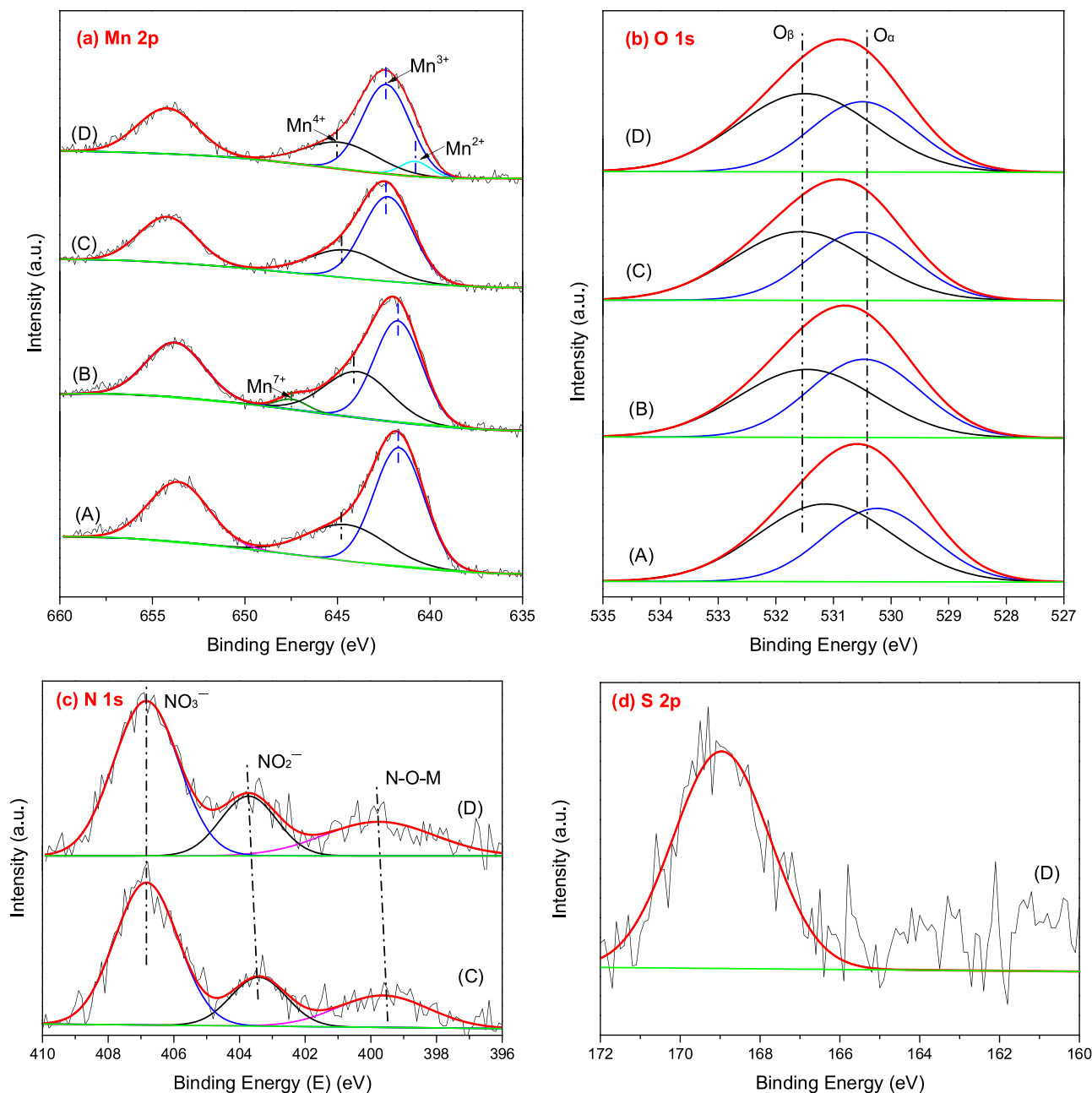| Sample	Mn^{2+}	Mn^{3+}	Mn^{4+}	Mn^{7+}	Mn^{2+}/Mn	Mn^{3+}/Mn	Mn^{4+}/Mn	Mn^{7+}/Mn
(A)	/	641.7	644.5	/	/	0.67	0.33	/
(B)	/	641.7	643.9	647.4	/	0.59	0.37	0.04
(C)	/	642.3	644.5	/	/	0.67	0.33	/
(D)	640.8	642.4	644.9	/	0.07	0.64	0.29	/

Fig. 7. XPS spectra of Mn 2p, O 1s, N 1s, and S 2p for fresh Mn/AlO$_x$ catalyst (A), after ozone decomposition (B), after deep oxidation without SO$_2$ (C), after deep oxidation with SO$_2$ (D).

Table 2
The binding energies (eV) and distribution of oxygen species.

Sample	O$_\alpha$	O$_\beta$	O$_\beta$/O$_\alpha$
(A)	530.2	531.1	1.30
(B)	530.5	531.5	1.07
(C)	530.5	531.6	1.30
(D)	530.5	531.5	1.44

second ozone decomposition pathway. As a result, O$_\beta$ will increase when the first adsorption mechanism is dominant, while O$_\alpha$ will increase when the second ozone decomposition mechanism dominates. It can be tentatively concluded that the second mechanism is the primary reaction pathway for the ozone decomposition process. Similar to the results found for the valence states of manganese, the ratio of O$_\beta$/O$_\alpha$ for the catalyst after deep oxidation without

SO$_2$ (sample (C)) shows no difference to the ratio measured for the fresh catalyst, supporting the previous conclusion. For the catalyst sample used in deep oxidation with SO$_2$ (sample (D)), the ratio of O$_\beta$/O$_\alpha$ increases compared to the fresh catalyst. SO$_2$ attaches to the metal oxides through Eq. (17), generating SO$_3$ or sulphates (indicated below) which remain on the catalyst surface, thus increasing the chemisorbed oxygen component. The electronic distribution becomes unbalanced due to sulphate formation, generating more vacancies to adsorb oxygen species [51].

The N 1s photoelectron spectra from the catalyst after deep oxidation with SO$_2$ (curve (C)) and without SO$_2$ (curve (D)) are shown in Fig. 7(c). The N 1s region is also resolved into sub-bands by the optimal Gaussian peak-fit method. Three peaks corresponding to N-O-Mn [52], NO$_2^-$ [53,54], and NO$_3^-$ [55] can be observed. N-O-Mn represents nitrogen species that have bonded with the metals, which are well distributed in the lattice structure, whereas the

Table 3
The binding energies (eV) and distribution of nitrogen species.

Sample	N-O-M	NO_2^-	NO_3^-	N-O-M/N	NO_2^-/N	NO_3^-/N
(C)	399.6	403.4	406.8	0.20	0.18	0.62
(D)	399.8	403.7	406.8	0.21	0.20	0.59

Table 4
Integrated area (a.u. × E8) of TPD signals for different catalyst samples.

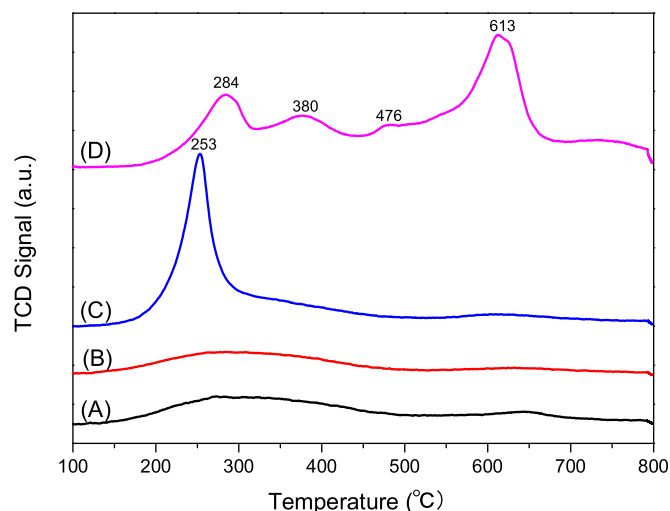| Sample	NO	NO_2	O_2 (70–700 °C)	SO_2
(C)	188	1.80	79.84	/
(D)	133	1.28	52.76	79.4
(F)	104	0.73	49.44	/
(G)	19.7	0.90	22.75	64.6

Fig. 8. H_2-TPR profiles for fresh Mn/AlO$_x$ catalyst (A), after ozone decomposition (B), after deep oxidation without SO_2 (C), after deep oxidation with SO_2 (D).

NO_2^-, derived from the NO_2–Mn, and NO_3^-, transferred from the NO_3–Mn, are distributed as chemisorbed species. The binding energies and ratios of these nitrogen species are listed in Table 3. It can be seen that the major nitrogen specie formed after deep oxidation is NO_3^-, with the concentrations of NO_2^- and N-O-Mn being approximately equal. A little decrease in NO_3^- is observed when the deep oxidation process includes SO_2, which may be from substitution of nitro species by sulphates. For the catalyst after deep oxidation with SO_2, sulfur species can be detected in the XPS spectrum, shown in Fig. 7(d). Only one peak with a binding energy of 168.9 eV can be observed, which can be assigned to inorganic sulphate with ionic S–O bands [56].
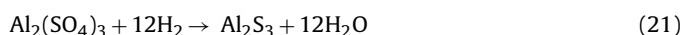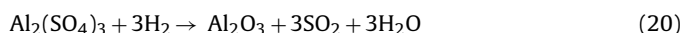
3.3.3. H_2-TPR

To investigate the variation of catalyst redox ability after application in ozone decomposition and deep oxidation, H_2-TPR measurements were performed (Fig. 8). For the fresh catalyst (curve (A)), there is a reduction region between 100 °C and 450 °C corresponding to the reduction of MnO_2 and Mn_2O_3 to Mn_3O_4 [57], and a smaller reduction region between 600 °C and 700 °C assigned to the reduction of MnO$_x$ species with larger particles [57]. There is no discernable difference between the H_2-TPR curve for the catalyst after ozone decomposition (curve (B)) and the fresh catalyst. However, for the catalyst used in deep oxidation of neat NO/N_2 (curve (C)), a large reduction peak appears at 253 °C, which is assigned to the reduction of nitrates. Four reduction peaks at 284 °C, 380 °C, 476 °C, and 613 °C can be observed for the catalyst used for deep oxidation with SO_2 (curve (D)). The lowest temperature peak comes from reduction of nitrate species, while the remaining peaks are attributed to the reduction of SO_4^{2-}. The H_2 reduction for bulk $MnSO_4$ is reported to occur between 540–800 °C [58], via Eq. (19); the improved dispersion of the $MnSO_4$ species leads to the lower reduction temperatures [59]. The H_2 reduction temperature range for bulk $Al_2(SO_4)_3$ is between 430–800 °C [58], via Eq. (20) and (21) [60]. Kijlstra et al. [60] investigated H_2-TPR of sulphated γ-Al_2O_3 and MnO_2, and found reduction temperatures between 407–507 °C for γ-Al_2O_3, and at 538 °C for MnO_2. It can be concluded

that the reduction peaks of 380 °C and 476 °C are associated with chemisorbed sulphates which are weakly bound, and the reduction peak at 613 °C may arise from bulk sulphates. It can be found by comparing samples (C) and (D) that the H_2 consumption, determined from the nitrates reduction peak area, is markedly reduced for the catalyst used with SO_2; additionally, a sample (D) features a peak corresponding to the reduction of sulphates associated with the alumina support matrix (Eq. (21)).

$$2MnSO_4 + 5H_2 \rightarrow MnO + MnS + SO_2 + 5H_2O \qquad (19)$$

$$Al_2(SO_4)_3 + 3H_2 \rightarrow Al_2O_3 + 3SO_2 + 3H_2O \qquad (20)$$

$$Al_2(SO_4)_3 + 12H_2 \rightarrow Al_2S_3 + 12H_2O \qquad (21)$$

3.3.4. TGA

TGA measurements were performed to investigate the catalyst weight loss as a function of temperature and determine the various compounds on the catalyst surface. The resultant TGA curves and derivative curves (DTA) are shown in Fig. 9. Three weight loss peaks can be observed for samples (C) and (F), and four peaks for samples (D) and (G). The first peak in all four samples is from the desorption of water vapor, hydroxyls, and weakly adsorbed nitrogen species, which are likely attached to low acidity surface hydroxyl groups. The second peak can be assigned to the decomposition of nitrates and nitrites. The transformation of MnO_2 to Mn_2O_3 is the foremost contribution to the third peak. The last peak at ~900 °C may be assigned to the decomposition of sulphates [60,61], with a small contribution from the phase transition [62] of metal oxides. The second and last peaks are those that are significant in the catalytic activity, and can be used to compare the quantity of nitrates, nitrites, and sulphates formed on the catalyst.

The TGA/DTA curve has been divided into three regions delineated by vertical dot-dash lines in Fig. 9, mass loss values have been given near their source peak. The first region below 285 °C is the previously mentioned dehydration peak. The second region is between 285–700 °C and results from the loss of nitrites and nitrates as well as mass change from the transformation of MnO$_x$; the transformation of MnO$_x$ is common to all four samples. The order of weight loss for the second region, is C > D > F > G. From this it can be concluded that: (1) the formation of nitrates and nitrites is inhibited by the addition of SO_2, as C > D and F > G; (2) ozone improves the adsorption of nitrogen species by the catalyst (C > F), even when SO_2 is present (D > G). For the third region, above 700 °C, the weight loss occurs from the loss of sulphates, samples (D) and (G) give the large signal. It can be seen that the weight loss for sample (G) is less than sample (D), implying that the ozone improves the adsorption of sulfur species on the catalyst.

3.3.5. TPD

TPD tests were carried out for the four catalyst samples in order to measure the desorption of NO, NO_2, O_2, and SO_2 from the catalyst during the heating process, with results shown in Fig. 10. The integrated areas of the four species for each catalyst sample are listed in Table 4. The O_2 desorption amounts given in Table 4 consider only the O_2 curve generated between 70–700 °C to avoid the interference from sulphate decomposition.

NO is the most abundant form of adsorbed nitrogen oxide. NO and NO_2 desorption traces can be roughly divided into two regions.
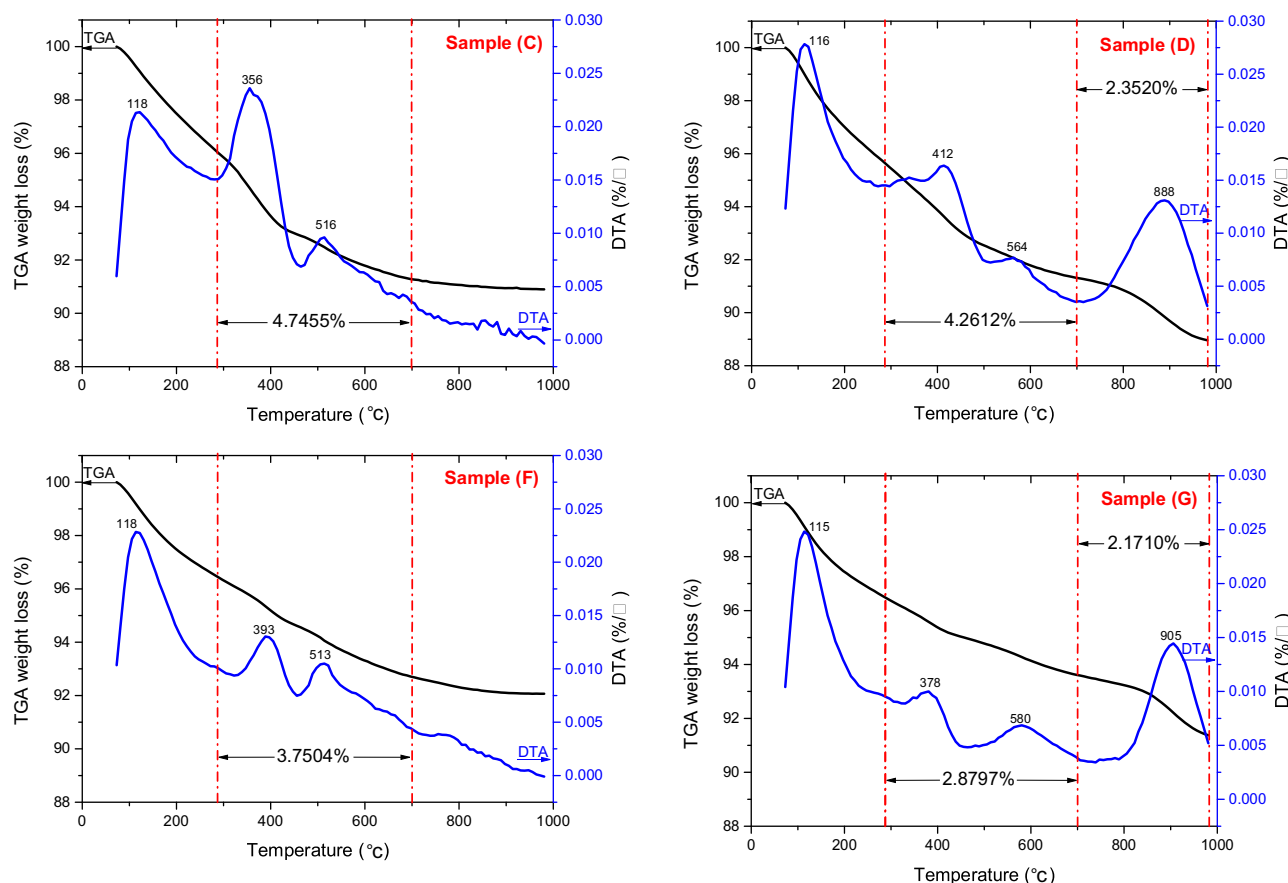
Fig. 9. TGA and DTA profiles for catalysts after deep oxidation without SO$_2$ (C), after deep oxidation with SO$_2$ (D), after adsorption of NO and O$_2$ (F), after adsorption of NO, O$_2$, and SO$_2$ (G).

The first desorption region between 130–280 °C, can be assigned to the weakly adsorbed nitrogen species on the surface, including bridging nitrate and nitrite species [63,64], the second peak between 280–420 °C is associated with monodentate and bidentate nitrate species [65,66]. The decomposition of these nitrates or nitrites, as well as adsorbed oxygen species correlate with the desorption of O$_2$ below 420 °C. The transformation of MnO$_2$ to Mn$_2$O$_3$, as mentioned above, gives rise to the third O$_2$ desorption peak above 420 °C. The SO$_2$-TPD results shown in Fig. 10(d) are consistent with the TGA results. The desorption peaks are found at 878 °C and 907 °C for samples (D) and (G), respectively. The decomposition temperatures reported for bulk MnSO$_4$ and Al$_2$(SO$_4$)$_3$ are 850 °C and 770 °C [67], respectively, while the decomposition temperatures for surface sulphates are somewhat lower. Evidently, the sulphates exist as the bulk form. Although sample (G) yields a higher maximum for its desorption peak than sample (D), the SO$_2$ desorption amount of sample (D) is greater, as listed in Table 4. This indicates that ozone weakens the bond between sulphates and metals oxides, but also enhances the formation of sulphates. The O$_2$ desorption peaks at temperatures above 700 °C result from the decomposition of sulphates, with the corresponding peaks in the SO$_2$ curve.

The mass release of NO, NO$_2$, and O$_2$ desorption for the catalyst sample trends as C > D > F > G (ignoring the insignificant NO$_2$ levels for sample (F) and (G)). This order is in agreement with TGA results, supporting the conclusions made above. To reiterate, the presence of ozone improves the adsorption of NO$_x$ and O$_2$, as the results of samples (C) and (F), especially in the presence of SO$_2$, as the results of samples (D) and (G) indicate. This provides explanation for the better resistance to SO$_2$ of the catalytic deep oxidation of

NO by ozone when compared with the catalysts used in catalytic oxidation of NO by O$_2$.

3.3.6. FTIR

The species formed on the catalyst surface by catalytic ozonation and adsorption were detected with FTIR, shown in Fig. 11(a). The bands at 1633/1634 cm^{-1} are ascribed to bridging nitrate [65,68] or residual bohmite AlO(OH). The bands at 1384/1385 cm^{-1} are assigned to free nitrates [69], including bidentate nitrate [70], monodentate nitrate [71], and ionic nitrate [71]. The intensity of the band decreases in the order C > D > F > G. The small bands at 1049 cm^{-1} for sample (C) and 1262 cm^{-1} for sample (F) are attributed to bridging nitrate [63], and bidentate nitrate [71], respectively. As shown in Fig. 11(b), these bands, which are associated with nitrates, disappear or diminish for samples after heating, showing these nitrates are decomposed above 500 °C. This is in agreement with TGA and TPD results. It can be observed that the bands at 1050 cm^{-1}, corresponding to sulphate species [72], are retained even after heating.

3.3.7. Porous structure measurements

Surface area is an important factor in catalytic processes. The porous structure parameters of the catalyst samples are characterized and listed in Table 5. Comparing with bare spherical alumina (sample (E)), the deposition of manganese oxides (sample (A)) leads to a decline in BET surface area, an increase in the average pore diameter, but little change in the total pore volume. The deposition process occupies some of the pores yielding these results. The accumulation of active oxygen species on the catalyst surface during the catalytic decomposition of ozone causes a decrease in surface area
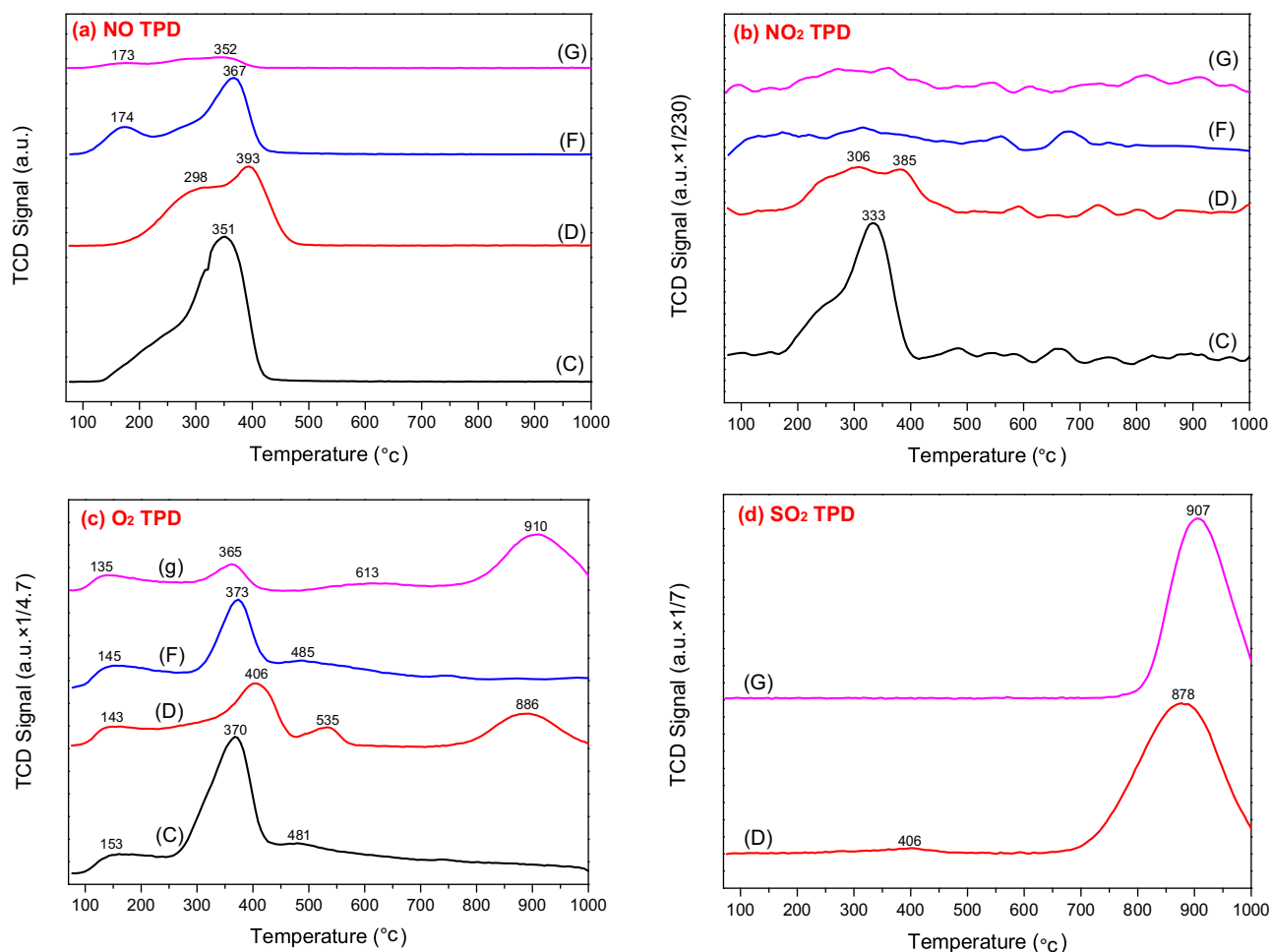
Fig. 10. TPD profiles of NO, NO_2, O_2, and SO_2 for catalysts after deep oxidation without SO_2 (C), after deep oxidation with SO_2 (D), after adsorption of NO and O_2 (F), after adsorption of NO, O_2, and SO_2 (G).
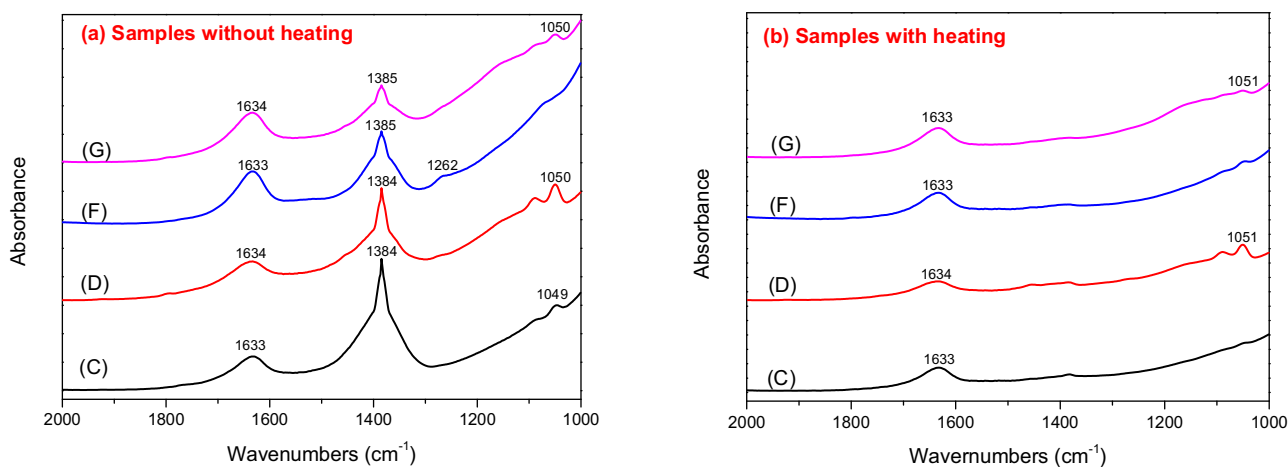

Fig. 11. FTIR spectra for catalysts after ozone decomposition (B), after deep oxidation without SO_2 (C), after deep oxidation with SO_2 (D), after adsorption of NO and O_2 (F), after adsorption of NO, SO_2, and O_2 (G). (a) the original samples, (b) the samples after heated to 500 °C.

for sample (B). The surface area after catalytic ozonation (sample (C)) returns to the level of the fresh catalyst (sample (A)), which is attributed to the consumption of active oxygen species by nitrogen oxides. A little decrease in surface area is also observed for sample (C) owing to the accumulation of nitrates and nitrites. Formation of sulphates on the catalyst (sample (D)) leads to more reduction of surface area than seen in the absence of SO_2, corresponding to retention of sulphates by the catalyst exposed to SO_2.

Table 5
Porous structure parameters of catalysts.

Sample	BET surface area (m^2/g)	Total pore volume (mL/g)	Average pore diameter (nm)
(A)	268.3	0.38	5.6
(B)	239.9	0.35	5.9
(C)	263.0	0.38	5.8
(D)	253.9	0.36	5.7
(E)	294.3	0.37	5.1

4. Conclusions

The catalytic activity of a catalyst for the deep oxidation of NO by ozone was evaluated. The catalyst, which was prepared by loading MnO$_x$ on spherical alumina substrate, increased the conversion efficiency of NO to N$_2$O$_5$ in comparison to non-catalytic deep oxidation. The use of this catalyst reduced the required residence time, the ozone requirement concentration and, by extension, ozone leakage. When O$_3$/NO$_x$ = 1.5, the NO$_2$ concentration was reduced from 600 ppm to 100 ppm at 100 °C for a residence time of 0.12 s, with an ozone leakage less than 20 ppm. The NO deep oxidation efficiency exceeded 95% for O$_3$/NO$_x$ > 1.57. The catalyst displayed good stability and resistance to SO$_2$. The catalyst also showed appreciable activity in ozone decomposition.

Two pathways for catalytic deep oxidation of NO by ozone were deduced. (1) Ozone decomposes into active oxygen atoms on the catalyst, which then react with NO$_2$ adsorbed on catalyst surface, producing NO$_3$ and other nitrates. N$_2$O$_5$ is then formed by the combination of adsorbed NO$_2$ and NO$_3$, which subsequently desorbed from the catalyst surface. (2) The manganese(III) is oxidized into manganese(IV) and manganese(VII) by ozone; in turn, the oxidized manganese ions oxidize NO$_2$ with subsequent reactions equivalent to the first mechanism. Characterization of the catalyst indicated that the second pathway is the most significant pathway in this catalytic ozonation process.

Catalyst characterization measurements, including XRD, XPS, H$_2$-TPR, TGA, TPD, FTIR, and BET, were performed for fresh catalyst, catalyst after deep oxidation, and after adsorption. The results illustrated that the presence of ozone enhanced the catalyst adsorption of NO$_x$, and O$_2$, especially with exposure to SO$_2$, which obviously contributed to the better performance regarding SO$_2$ poisoning compared with catalysts for NO oxidation by O$_2$.

Acknowledgments

References

[1] S. Dahlin, M. Nilsson, D. Bäckström, S.L. Bergman, E. Bengtsson, S.L. Bernasek, L.J. Pettersson, Appl. Catal. B: Environ. 183 (2016) 377–385.
[2] Y. He, M.E. Ford, M. Zhu, Q. Liu, U. Tumuluri, Z. Wu, I.E. Wachs, Appl. Catal. B: Environ. 193 (2016) 141–150.
[3] D.Q. Dao, L. Gasnot, K. Marschallek, A. El Bakali, J.F. Pauwels, Energy Fuel 24 (2010) 1696–1703.
[4] S.L. Ding, Q. Yu, Y.Z. Zhang, Y. Liu, C.X. Xie, G. Yu, J. Adv. Oxid. Technol. 18 (2015) 114–122.
[5] I. Jogi, E. Stamate, C. Irimiea, M. Schmidt, R. Brandenburg, M. Holub, M. Bonislawski, T. Jakubowski, M.L. Kaariainen, D.C. Cameron, Fuel 144 (2015) 137–144.
[6] K. Li, X.L. Tang, H.H. Yi, P. Ning, D.J. Kang, C. Wang, Chem. Eng. J. 192 (2012) 99–104.
[7] K. Skalska, J.S. Miller, S. Ledakowicz, Chem. Eng. Sci. 66 (2011) 3386–3391.
[8] Z.H. Wang, J.H. Zhou, Y.Q. Zhu, Z.C. Wen, J.Z. Liu, K. Cen, Fuel Process. Technol. 88 (2007) 817–823.
[9] C.H. Zheng, C.R. Xu, Y.X. Zhang, J. Zhang, X. Gao, Z.Y. Luo, K.F. Cen, Appl. Energy 129 (2014) 187–194.
[10] W.L. Chang, P.V. Bhave, S.S. Brown, N. Riemer, J. Stutz, D. Dabdub, Aerosol Sci. Technol. 45 (2011) 665–695.
[11] K. Skalska, J.S. Miller, S. Ledakowicz, Sci. Total. Environ. 408 (2010) 3976–3989.
[12] C.L. Sun, N. Zhao, Z.K. Zhuang, H.Q. Wang, Y. Liu, X.L. Weng, Z.B. Wu, J. Hazard. Mater. 274 (2014) 376–383.
[13] H. Huang, H. Huang, Y. Zhan, G. Liu, X. Wang, H. Lu, L. Xiao, Q. Feng, D.Y. Leung, Appl. Catal. B: Environ. 186 (2016) 62–68.
[14] G.G. Bessegato, J.C. Cardoso, B.F. da Silva, M.V.B. Zanoni, Appl. Catal. B: Environ. 180 (2016) 161–168.
[15] J. Nawrocki, B. Kasprzyk-Hordern, Appl. Catal. B: Environ. 99 (2010) 27–42.
[16] M.N. Dinh, J.-M. Giraudon, A. Vandenbroucke, R. Morent, N. De Geyter, J.-F. Lamonier, Appl. Catal. B: Environ. 172 (2015) 65–72.
[17] H. Einaga, N. Maeda, Y. Teraoka, Appl. Catal. B: Environ. 142 (2013) 406–413.
[18] H. Einaga, N. Maeda, S. Yamamoto, Y. Teraoka, Catal. Today 245 (2015) 22–27.
[19] H. Einaga, Y. Teraoka, A. Ogat, Catal. Today 164 (2011) 571–574.
[20] H. Einaga, Y. Teraoka, A. Ogata, J. Catal. 305 (2013) 227–237.
[21] L.P. Long, J.G. Zhao, L.X. Yang, M.L. Fu, J.L. Wu, B.C. Huang, D.Q. Ye, Chin. J. Catal. 32 (2011) 904–916.
[22] E. Rezaei, J. Soltan, N. Chen, Appl. Catal. B: Environ. 136 (2013) 239–247.
[23] H.C. Wang, H.S. Liang, M.B. Chang, J. Hazard. Mater. 186 (2011) 1781–1787.
[24] S. Dimitrova, G. Ivanov, D. Mehandjiev, Appl. Catal. A: Gen. 266 (2004) 81–87.
[25] P.C.C. Faria, J.J.M. Orfao, M.F.R. Pereira, Appl. Catal. B: Environ. 88 (2009) 341–350.
[26] J. Ma, M.H. Sui, Z.L. Chen, L.N. Wang, Ozone Sci. Eng. 26 (2004) 3–10.
[27] N. Blanch-Raga, A. Palomares, J. Martínez-Triguero, S. Valencia, Appl. Catal. B: Environ. 187 (2016) 90–97.
[28] H. Einaga, S. Futamura, J. Catal. 227 (2004) 304–312.
[29] I. Jõgi, K. Erme, J. Raud, M. Laan, Fuel 173 (2016) 45–51.
[30] Q. Ma, Z. Wang, F. Lin, M. Kuang, R. Whiddon, Y. He, J. Liu, Energy Fuel 30 (2016) 2302–2308.
[31] E. Rezaei, J. Soltan, Appl. Catal. B: Environ. 148 (2014) 70–79.
[32] C. Reed, Y. Xi, S.T. Oyama, J. Catal. 235 (2005) 378–392.
[33] J. Jia, P. Zhang, L. Chen, Appl. Catal. B: Environ. 189 (2016) 210–218.
[34] P. Konova, M. Stoyanova, A. Naydenov, D. Mehandjiev, Appl. Catal. A: Gen. 298 (2006) 109–114.
[35] W. Li, G.V. Gibbs, S.T. Oyama, J. Am. Chem. Soc. 120 (1998) 9041–9046.
[36] A. Nishino, Catal. Today 10 (1991) 107–118.
[37] B. Dhandapani, S.T. Oyama, Appl. Catal. B: Environ. 11 (1997) 129–166.
[38] J. Li, L. Li, W. Cheng, F. Wu, X. Lu, Z. Li, Chem. Eng. J. 244 (2014) 59–67.
[39] T. Hamzehlouyan, C.S. Sampara, J. Li, A. Kumar, W.S. Epling, Appl. Catal. B: Environ. 181 (2016) 587–598.
[40] T. Cwele, N. Mahadevaiah, S. Singh, H.B. Friedrich, Appl. Catal. B: Environ. 182 (2016) 1–14.
[41] F. Lin, Y. He, Z. Wang, Q. Ma, R. Whiddon, Y. Zhu, J. Liu, RSC Adv. 6 (2016) 31422–31430.
[42] H. Einaga, S. Futamura, React. Kinet. Catal. Lett. 81 (2004) 121–128.
[43] M. Wang, P. Zhang, J. Li, C. Jiang, Chin. J. Catal. 35 (2014) 335–341.
[44] W. Tang, X. Wu, S. Li, X. Shan, G. Liu, Y. Chen, Appl. Catal. B: Environ. 162 (2015) 110–121.
[45] M. Oku, J. Electron. Spectrosc. 74 (1995) 135–148.
[46] H. Zhang, J. Chen, P. Liang, L. Wang, J. Environ. Sci.: China 24 (2012) 2083–2090.
[47] C. Reed, Y.-K. Lee, S.T. Oyama, J. Phys. Chem. B 110 (2006) 4207–4216.
[48] P. Sudarsanam, B. Hillary, M.H. Amin, S.B.A. Hamid, S.K. Bhargava, Appl. Catal. B: Environ. 185 (2016) 213–224.
[49] V.P. Santos, M.F.R. Pereira, J.J.M. Orfao, J.L. Figueiredo, Appl. Catal. B: Environ. 99 (2010) 353–363.
[50] P. Venkataswamy, K.N. Rao, D. Jampaiah, B.M. Reddy, Appl. Catal. B: Environ. 162 (2015) 122–132.
[51] X.S. Du, X. Gao, L.W. Cui, Y.C. Fu, Z.Y. Luo, K.F. Cen, Fuel 92 (2012) 49–55.
[52] F. Dwikusuma, T.F. Kuech, J. Appl. Phys. 94 (2003) 5656–5664.
[53] P.W. Wang, J.-C. Hsu, Y.-H. Lin, H.-L. Chen, Appl. Surf. Sci. 256 (2010) 4211–4214.
[54] C.K. Hwangbo, L.J. Lingg, J.P. Lehan, H.A. Macleod, F. Suits, Appl. Opt. 28 (1989) 2779–2784.
[55] Ş. Sayan, Ş. Süzer, D. Uner, J. Mol. Struct. 410 (1997) 111–114.
[56] S.J. Yang, Y.F. Guo, H.Z. Chang, L. Ma, Y. Peng, Z. Qu, N.Q. Yan, C.Z. Wang, J.H. Li, Appl. Catal. B: Environ. 136 (2013) 19–28.
[57] V. de la Peña O'Shea, J. Alvarez-Galvan, J. Fierro, P. Arias, Appl. Catal. B: Environ. 57 (2005) 191–199.
[58] F. Habashi, S.A. Mikhail, K.V. Van, Can. J. Chem. 54 (1976) 3646–3650.
[59] E.N. Bjoernbom, S. Druesne, M.F. Zwinkels, S.G. Jaeraas, Ind. Eng. Chem. Res. 34 (1995) 1853–1858.
[60] W.S. Kijlstra, M. Biervliet, E.K. Poels, A. Bliek, Appl. Catal. B: Environ. 16 (1998) 327–337.
[61] Y. Li, M.Q. Shen, J.Q. Wang, T.M. Wan, J. Wang, Catal. Sci. Technol. 5 (2015) 1731–1740.
[62] J. Cheng, J. Yu, X. Wang, L. Li, J. Li, Z. Hao, Energy Fuel 22 (2008) 2131–2137.
[63] D. Meng, W. Zhan, Y. Guo, Y. Guo, L. Wang, G. Lu, ACS Catal. 5 (2015) 5973–5983.
[64] M. Machida, D. Kurogi, T. Kijima, Chem. Mater. 12 (2000) 3165–3170.
[65] S. Kameoka, Y. Ukisu, T. Miyadera, Phys. Chem. Chem. Phys. 2 (2000) 367–372.
[66] X. Zhang, H. He, H. Gao, Y. Yu, Spectrochim. Acta A 71 (2008) 1446–1451.
[67] R.C. Weast, CRC Press, Inc. 1977, F231–F235.

[68] M.P. Ruggeri, I. Nova, E. Tronconi, J.A. Pihl, T.J. Toops, W.P. Partridge, Appl. Catal. B: Environ. 166 (2015) 181–192.

[69] Z. Wang, F. Lin, S. Jiang, K. Qiu, M. Kuang, R. Whiddon, K. Cen, Fuel 166 (2016) 352–360.

[70] W. Wang, G. McCool, N. Kapur, G. Yuan, B. Shan, M. Nguyen, U.M. Graham, B.H. Davis, G. Jacobs, K. Cho, Science 337 (2012) 832–835.

[71] Q. Li, M. Meng, Z.-Q. Zou, X.-G. Li, Y.-Q. Zha, J. Hazard. Mater. 161 (2009) 366–372.

[72] A. Kustov, M.Y. Kustova, R. Fehrmann, P. Simonsen, Appl. Catal. B: Environ. 58 (2005) 97–104.